Thermoelectric Properties of $Cu_2Se_{1-x}Te_x$ Solid Solutions

Kunpeng Zhao[1,2], Mengjia Guan[1,2], Pengfei Qiu[1], Anders B. Blichfeld[3,4], Espen Eikeland[3], Chenxi Zhu[1], Dudi Ren[1], Fangfang Xu[1], Bo B. Iversen[3], Xun Shi[1], and Lidong Chen[1*]*

1 State Key Laboratory of High Performance Ceramics and Superfine Microstructure, Shanghai Institute of Ceramics, Chinese Academy of Sciences, Shanghai 200050, China.

2 University of Chinese Academy of Sciences, Beijing 100049, China.

3 Centre for Materials Crystallography, Department of Chemistry and iNANO, Aarhus University, Langelandsgade 140, DK-8000 Aarhus C, Denmark.

4 Department of Materials Science and Engineering, Norwegian University of Science and Technology, N-7491 Trondheim, Norway.

* Corresponding author. E-mail: xshi@mail.sic.ac.cn and cld@mail.sic.ac.cn

Abstract

Binary Cu_2Se and Cu_2Te have gained a great attention recently because of their interesting and abnormal physical properties, such as ultralow thermal conductivity, high carrier mobility, large effective mass of carriers and excellent thermoelectric performance. In this study, we find these two compounds are completely miscible throughout the studied composition range. The trigonal structure of Cu_2Se is maintained when the Te content x is 0.2, but a new trigonal structure is formed when the Te content x is between 0.3 and 0.7. The carrier concentration is greatly improved when increasing the Te content in $Cu_2Se_{1-x}Te_x$ solid solutions, resulting in much reduced electrical resistivity and Seebeck coefficient in the whole temperature range as compared with those of binary Cu_2Se. The total thermal conductivity is inversely increased due to the contribution from enhanced carrier thermal conductivity. As a result, the overall thermoelectric performance of $Cu_2Se_{1-x}Te_x$ solid solutions lies between Cu_2Se and Cu_2Te. We also find that the quality factor of $Cu_2Se_{1-x}Te_x$ is higher than most typical thermoelectric materials. Thus, the thermoelectric performance can be further improved if the intrinsically high hole carrier concentrations can be reduced in $Cu_2Se_{1-x}Te_x$.

Introduction

Thermoelectric (TE) materials, which can directly convert heat into electricity and vice versa, have attracted widespread research interests due to its advantages of no moving parts, no mechanical or chemical processes involved, emission free, high durability and reliability.[1-4] TE technology shows a great potential in a variety of applications such as cooling and power generation using waste heat resources.[5] Their energy conversion efficiency is characterized by the dimensionless figure of merit, defined as $zT = S^2T/(\rho\kappa)$, where S, T, ρ, and κ are the Seebeck coefficient, absolute temperature, electrical resistivity, and total thermal conductivity (including lattice contribution κ_L and carrier contribution κ_c), respectively. The κ_L can be tuned indpendently sometimes and the other parameters S, ρ, and κ_c, however, are strongly interrelated through material carrier concentrations and/or electronic structures.[6] Thus, good TE materials are expected to possess an ideal crystal structure with two independent structural units that can be used to separate the interrelation between electrical and thermal transports. In order to realize this idea, the concept of phonon-glass electron-crystal (PGEC),[7] introduced by G. A. Slack, shows that an efficient thermoelectric material should exhibit low thermal conductivity as that in a glass but high electricity as that in a well-ordered crystal. Based on the PGEC concept, various good TE materials with high *zTs* have been reported, including filled skutterdites,[8, 9] zintl phases,[10, 11] and clathrates.[12, 13] Recently, the PGEC concept is further extended to superionic conductors within a name of phonon-liquid electron-crystal (PLEC).[14] The crystal structure of the PLEC material has two typical sublattices. One is the rigid and crystalline sublattice made by anion atoms. Another is the liquid-like sublattice made by cations that are around the anion sublattice with the ability of hopping (flowing) between the symmetry equivalent atomic sites. The disordered and mobile cations lead to ultralow κ_L beyond the limit value in a glass not only by reducing the phonon mean free path but also by eliminating some of the phonon vibration modes.[14]

As the most typical PLEC material, copper chalcogenides $Cu_{2-\delta}X$-based (X = S, Se, and Te) compounds have demonstrated excellent TE performances with the peak *zT*s above 2,[15-21] comparable to or exceeding many state-of-the-art TE materials reported before. In spite of their simple chemical compositions, the crystal structures of copper chalcogenides are actually quite complex, which depend sensitively on the amount of Cu deficiency δ and fabrication process.[17, 22] The room temperature structures of $Cu_{2-\delta}Se$, $Cu_{2-\delta}S$, and $Cu_{2-\delta}Te$ are diverse from each other, and

a variety of possible crystal structures have been proposed by previous researchers.[23-27] However, the clear-cut crystal structure remains a controversial issue. For example, the low temperature crystal structure of Cu_2Se has been proposed divergently to be either monoclinic,[23] or orthorhombic,[24] or tetragonal structures.[25] Specially, a trigonal structure with much higher symmetry $R\bar{3}m$ is proposed by Espen recently, based on analysis of single crystal X-ray diffraction data.[28] Upon heating, the complicated room temperature $Cu_{2-\delta}X$ phase gradually converts to the high-temperature phases. But the phase transition temperatures and numbers are determined by δ. Specifically, the stoichiometric Cu_2Se, Cu_2S, and Cu_2Te coumpounds experience 1, 2, and 5 phase transitions, respectively, from 300 K to 900 K.[15, 21, 28] The final cubic phase of $Cu_{2-\delta}X$ is an superionic conductor, where the anion X^{2-} occupy positions on the face-centered cubic sublattice and the Cu^+ ions are kinetically distributed over multiple sites with a mobility like a liquid. The exact location of Cu^+ ions is actually not the same for different $Cu_{2-\delta}X$ compounds, or even in controversy for the same $Cu_{2-\delta}X$ compound,[29] due to the nature of surperionic conductors. In spite of the complexity and uncertainty of crystal structure, it is surprising to note that the $Cu_{2-\delta}X$ matrix can form solid solutions between each other. He et al. reported that Cu_2S and Cu_2Te form a complete solid solution with special mosaic crystal microstructure wherein the nanoscale grains are highly aligned,[30] resulting in an ultrahigh zT of 2.1 at 1000 K. Zhao et al. found Cu_2Se and Cu_2S also form solid solutions,[31, 32] which possess the good electrical transport properties stemming from Cu_2Se and the low lattice thermal conductivity from Cu_2S, and thereby reaching an outstanding zT value. Via powder X-ray diffraction analyses, Gasimova and Alieva studied the structural phase transitions of $Cu_2Se_{1-x}Te_x$ (x= 0.25 and 0.5) solid solutions between Cu_2Se and Cu_2Te.[33, 34] However, the exact atomic positions for $Cu_2Se_{1-x}Te_x$ are still unknown and their thermoelectric properties have not been studied. Thus, a detailed study of the crystal structure and thermoelectric transport properties for $Cu_2Se_{1-x}Te_x$ is still desirable.

Herein we successfully synthesized a series of $Cu_2Se_{1-x}Te_x$ (x= 0.2, 0.3, 0.5, 0.7) solid solutions by melting-annealing approach followed by spark plasma sintering. The detailed crystal structures are determined by single crystal structural solution, powder X-ray diffraction, and Rietveld refinements. Besides, the effects of Te alloying on the thermal and electrical transport properties have been systematically studied. Furthermore, the relationship among these physical properties has been deeply analyzed and the relevant mechanisms have been discussed.

Experimental Section

Synthesis. Polycrystalline samples with nominal compositions of $Cu_2Se_{1-x}Te_x$ with x = 0.2, 0.3, 0.5, and 0.7 were synthesized by a melting-annealing-sintering process. High purity elements Cu (shot, 99.999%, Alfa Aesar), Se (shot, 99.999%, Alfa Aesar), and Te (shots, 99.999%, Alfa Aesar) were loaded into Boron Nitride crucibles that were sealed in a fused silica tube under vacuum. The tubes were firstly raised to 1423 K with a rate of 100 K h^{-1} and kept at this temperature for 12 h, then slowly cooled down to 1073 K with a rate of 7 K h^{-1} and soaked at this temperature for 8 days, and finally cooled to room temperature naturally. Small single crystals were extracted from the as-prepared polycrystalline ingot samples. Some red copper precipitates were observed on the surface of the ingots for all samples. After removing these copper precipitates, the obtained ingots were crushed and grounded to fine powders using a mortar and pestle. Then the powders were loaded into a graphite die with a diameter of 10 mm and consolidated by spark plasma sintering (Sumitomo SPS-2040) at 873 K under a pressure of 65 MPa for 5 minutes. Electrically insulating and thermally conducting BN layers were sprayed onto the carbon foils and the inner sides of the graphite die before the SPS process in order to prohibit DC pulsed currents going through the powders. For comparison, the Cu_2Se and Cu_2Te were prepared using the same method.

Characterization. Single-crystal (about 10 × 40 × 60 μm^3) X-ray diffraction measurements were performed on a SuperNova diffractometer from Agilent Technologies using $Mo_{K\alpha}$ radiation (λ = 0.71073 Å). Diffracted intensities were collected on a CCD detector and the data were integrated and corrected for absorption using CrysAlisPro. The structure solution and refinement were carried out with SHELXT, using the Olex2 gui. Room-temperature powder X-ray diffraction data was recorded on Rigaku Rint 2000 with a Cu-K_α source (λ = 1.5406 Å). Full profile refinements by Rietveld analysis were carried out for $Cu_2Se_{1-x}Te_x$ samples using the program Full-Prof. High-temperature powder X-ray diffraction (HT-PXRD) data were collected at the beam line BL02B2 at Spring8, Japan. The sample morphologies were measured by field emission scanning electron microscopy (FESEM, Magellan-400) equipped with energy dispersive X-ray analysis (EDS, Horiba 250). The TEM examination was performed on a JEM-2100F field-emission transmission electron microscope. The sound speed data were obtained by use of

ultrasonic measurement system UMS-100 with shear wave transducers of 5 MHz and longitudinal wave transducers of 10 MHz. The electrical resistivity (ρ) and Seebeck coefficient (S) were measured simultaneously using a commercial system (ULVAC ZEM-3). Thermal diffusivity (D) was measured using the laser flash method (Netzsch, LFA-457). The specific heat (C_p) was determined by differential scanning calorimetric using Netzsch DSC 404F3. The density (d) was measured by the Archimedes method and the relative density of bulk $Cu_2Se_{1-x}Te_x$ samples was higher than 98%. The total thermal conductivity (κ) was calculated according to the relationship $\kappa = dC_pD$. The Hall coefficient (R_H) at 300 K was measured using a physical properties measurement system (PPMS-9, Quantum Design, USA) with a magnetic field swept from -3 to 3 T. The hall carrier concentration (p) and carrier mobility μ_H were calculated by $p = 1/R_He$ and $\mu_H = R_H/\rho$, respectively, where e is the elementary charge.

Results and Discussion

Single-crystal X-ray diffraction was used to solve the crystal structures of $Cu_2Se_{0.8}Te_{0.2}$ and $Cu_2Se_{0.5}Te_{0.5}$ at 100 K. The obtained crystallographic information is listed in Table 1. Both samples have trigonal structure with space group of $R\bar{3}m$, which is the same as the one in Cu_2Se proposed recently. The Se/Te sites are fully occupied, whereas the Cu sites are partially occupied. The number of Cu sites is not the same between $Cu_2Se_{0.8}Te_{0.2}$ and $Cu_2Se_{0.5}Te_{0.5}$, resulting in different crystal structures, which will be discussed below. Besides, weak super-structure reflections (**Figure 1**) are observed in the diffraction data for the solid solution materials, indicating a 3×3×1 super cell existed in the material. Similar phenomenon has been also observed in Cu_2Se and Cu_2Te matrix compounds.[35, 36] The average structure of $Cu_2Se_{0.8}Te_{0.2}$ is displayed in **Figure 2a**. It is the same as the structure of Cu_2Se, but it has slightly larger cell parameters with the values of a = 4.1400(6) Å and c = 20.592(5) Å at 100 K. The structure consists of one shared Se/Te atomic site and two disordered copper sites (Cu1 & Cu2). The Se/Te atoms form the hexagonal close packed (cp) layers stacked along the c-axis, and the Cu atoms locate between every alternate layer. Thus this structure has sandwich-like feature with the character of alternating layers composed by one copper empty layer and one copper rich layer along the c-axis. The Cu1 site is split into three equivalent positions (Cu1a, Cu1b and Cu1c) that are located in the center of blue tetrahedron, as shown in Figure 2a. The Cu2 site is split into two positions (Cu2a and Cu2b)

that are situated slightly above and below the mirror plane of red octahedron. The structure of $Cu_2Se_{0.5}Te_{0.5}$ is almost the same as $Cu_2Se_{0.8}Te_{0.2}$. It also has the hexagonal chalcogenide framework and a sandwich-like feature that is composed of an almost copper empty layer and a copper rich layer. However, the *c* parameter in $Cu_2Se_{0.5}Te_{0.5}$ is doubled to 41.845(4) Å because there are two slightly different copper rich layers in the unit cell. The ultra-long *c* parameter is almost identical to the one (*c* = 41.8531 Å) in the hexagonal structure proposed by Alieva *et al.* refined using powder X-ray diffraction.[34] In Figure 2b, the polyhedrons with different colors are shown to highlight the different layers. The layers with blue tetrahedrons and red octahedrons are the same as the ones in $Cu_2Se_{0.8}Te_{0.2}$, but the green tetrahedrons and yellow octahedrons contain two new atomic sites Cu3 and Cu4. Cu3 has only one position located in the center of green tetrahedron, while Cu4 is split into two positions situated closing to the inner faces of the yellow octahedron.

Table 1. Crystallographic information for compounds $Cu_2Se_{0.8}Te_{0.2}$ and $Cu_2Se_{0.5}Te_{0.5}$.

Sample	$Cu_2Se_{0.8}Te_{0.2}$	$Cu_2Se_{0.5}Te_{0.5}$
Temperature	100 K	100 K
Crystal system	trigonal	trigonal
Space group	$R\bar{3}m$	$R\bar{3}m$
a/Å	4.1400(6)	4.1807(4)
b/Å	4.1400(6)	4.1807(4)
c/Å	20.592(5)	41.845(4)
α/°	90	90
β/°	90	90
γ/°	120	120
Volume/Å^3	305.7(1)	633.4(1)
Z	6	12
μ/mm^{-1}	36.658	36.046
F(000)	560.0	1248.0
$(\sin\theta/\lambda)_{max}$ /Å^{-1}	0.62	0.62
$N_{Tot,obs}$	1287	3143
$N_{Uniq,obs}$	104	212
GOF	1.217	1.180

R_{int}	0.103	0.069
$R_1, R_1[F^2 > 2\sigma(F^2)]$	0.045, 0.043	0.059, 0.057
$wR_2, wR_2[F^2 > 2\sigma(F^2)]$	0.105, 0,106	0.137, 0.135
$\Delta\rho_{max}, \Delta\rho_{min}$ (e Å^{-3})	2.04, -0.92	5.11, -3.62

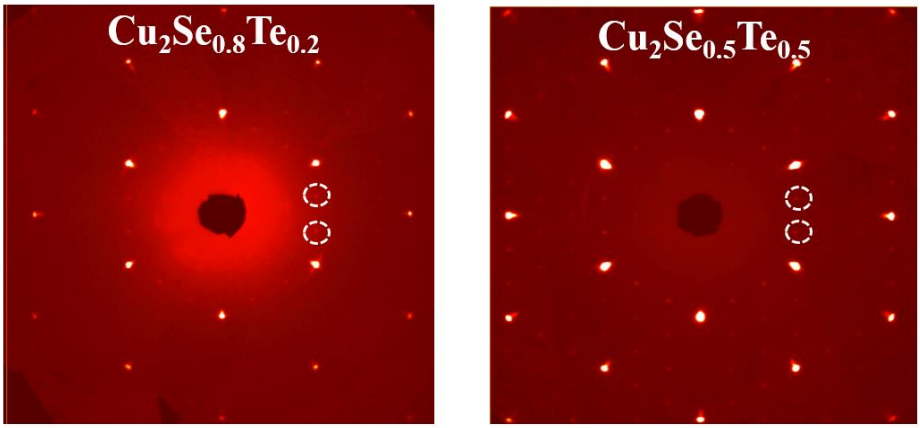

Figure 1. Single crystal X-ray diffraction patterns for $Cu_2Se_{0.8}Te_{0.2}$ and $Cu_2Se_{0.5}Te_{0.5}$ along [001] direction. The 3 × 3 × 1 super cell diffraction spots are marked by the white rings.

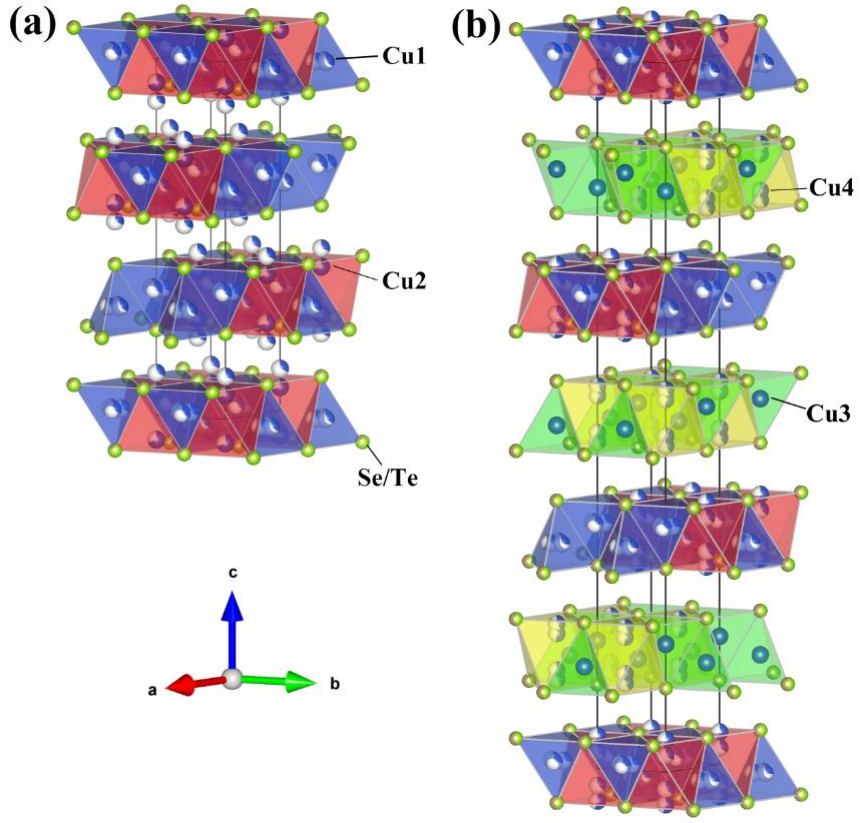

Figure 2. Visualization of the crystal structures ($R\bar{3}m$) of $Cu_2Se_{0.8}Te_{0.2}$ **(a)** and $Cu_2Se_{0.5}Te_{0.5}$ **(b)** obtained from single crystal structural solution at 100 K. The Cu1 sites, Cu2 sites, Cu3 sites, and

Cu4 sites are located in the blue tetrahedrons, red octahedrons, green tetrahedrons, and yellow octahedrons, respectively. The atomic site occupancy is indicated by partial coloring of the atoms.

The X-ray diffraction (XRD) patterns measured on powder $Cu_2Se_{1-x}Te_x$ (x= 0, 0.2, 0.3, 0.5, 0.7, and 1.0) samples are depicted in **Figure 3a**. The XRD pattern of $Cu_2Se_{0.8}Te_{0.2}$ is nearly the same as Cu_2Se, indicating no structural change. However, with increasing the Te content *x* to above 0.3, the XRD patterns of $Cu_2Se_{1-x}Te_x$ are significantly changed. Almost all diffraction peaks of $Cu_2Se_{0.7}Te_{0.3}$, $Cu_2Se_{0.5}Te_{0.5}$, and $Cu_2Se_{0.3}Te_{0.7}$ are clearly indexed by the new trigonal structures described above. The Te^{2-} ions (221 pm) have a larger ionic radius than Se^{2-} (198 pm), thus an expansion of the unit cell is expected upon substitution of Se with Te. This is clearly demonstrated in Figure 3b, in which the lattice parameters increase when increasing Te content. For comparison, half of the *c* parameter for *x* = 0.3, 0.5 and 0.7 and thrice the *c* parameter for Cu_2Te are shown in Figure 3b. The non-linear dependence could be attributed to the different crystal structures in these materials.

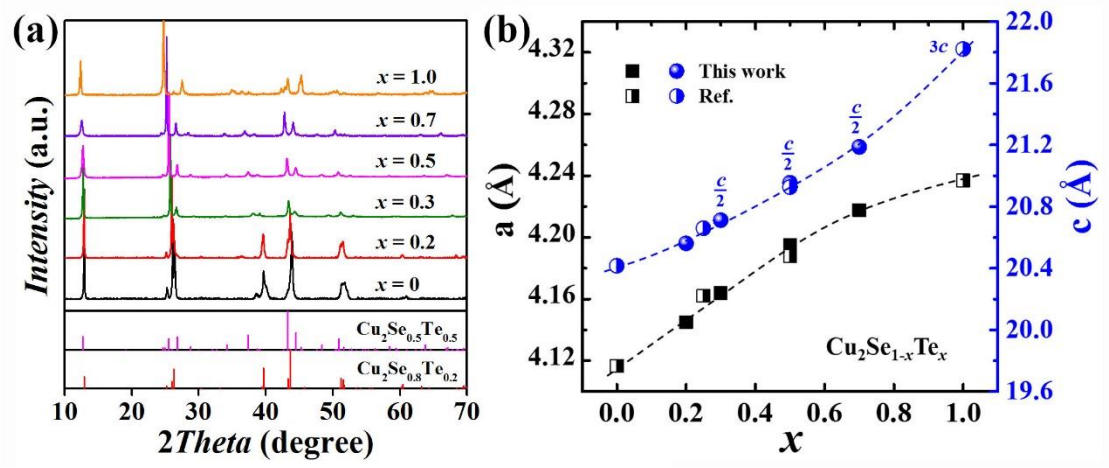

Figure 3. (a) Powder X-ray diffraction patterns for $Cu_2Se_{1-x}Te_x$ (x= 0.2, 0.3, 0.5, 0.7) at room temperature. **(b)** The lattice parameter (*a* & *c*) as a function of Te concentration. The data of Cu_2Se, $Cu_2Se_{0.75}Te_{0.25}$, $Cu_2Se_{0.5}Te_{0.5}$, and Cu_2Te from literatures[28, 33, 34, 37] are included for comparison. The dashed lines are guide to the eyes.

Table 2 Refined parameters and quality factors based on the PXRD data for $Cu_2Se_{1-x}Te_x$ (x = 0.2, 0.3, 0.5, and 0.7) at room temperature. The data of Cu_2Se and Cu_2Te are taken from refs. 26 and

35.

Sample	Phase	Space group	*a* (Å)	*c* (Å)	R_p (%)	R_{wp} (%)	χ^2
Cu_2Se	Trigonal	*R-3m*	4.1167	20.4160			
$Cu_2Se_{0.8}Te_{0.2}$	Trigonal	*R-3m*	4.1449	20.5614	1.9726	2.6444	1.6933
$Cu_2Se_{0.7}Te_{0.3}$	Trigonal	*R-3m*	4.1638	41.4230	4.8281	7.9704	5.1873
$Cu_2Se_{0.5}Te_{0.5}$	Trigonal	*R-3m*	4.1949	41.9092	3.3676	5.9993	3.5428
$Cu_2Se_{0.3}Te_{0.7}$	Trigonal	*R-3m*	4.2177	42.3735	5.4650	8.6633	4.0578
Cu_2Te	Hexagonal	*P6/mmm*	4.237	7.274			

The microstructural features of $Cu_2Se_{0.5}Te_{0.5}$ were investigated using scanning electron microscopy (SEM) and transmission electron microscopy (TEM) techniques. The typical layered cleavage plates with the thickness ~100 nm are clearly observed, which is consistent with the sandwich-like crystal structure solved by single-crystal X-ray diffraction shown above. The elemental mapping and the backscattered electron microscopy (BSE) images are shown in **Figure 4b**. All elements distributed homogeneously in the materials without any element accumulations and impurity phases. Furthermore, a lot of nanograins, distorted lattices, and dislocations were observed by high resolution transmission electron microscopy (HRTEM), as shown in Figure 4c and 4d. These nanostructural defects are propitious to scatter lattice phonons for low thermal conductivity.

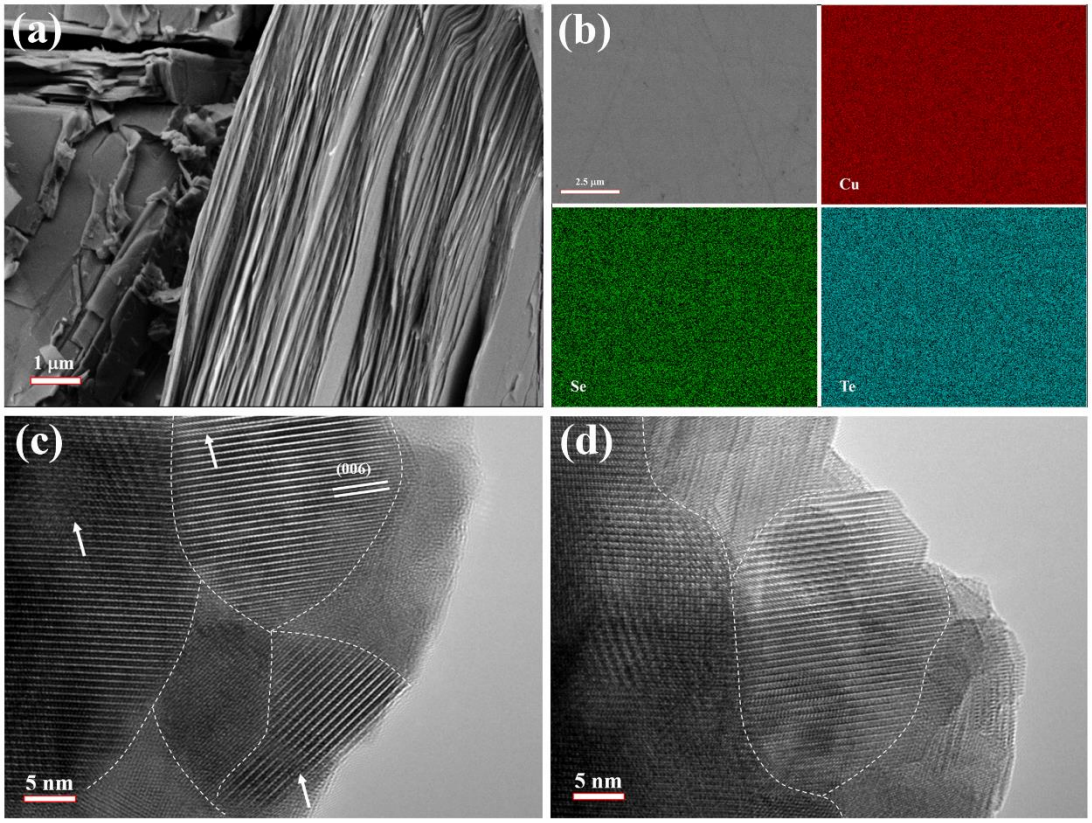

Figure 4. Microstructures for the sintered sample $Cu_2Se_{0.5}Te_{0.5}$. **(a)** Fractured secondary electron (SE) image. **(b)** Backscattered electron microscopy (BSE) image and elemental energy-dispersive X-ray spectroscopy (EDS) mapping. **(c, d)** High resolution TEM images.

As mentioned above, Cu_2Se undergoes one structural transformation while Cu_2Te has five phase transitions above room temperature. Thus it is necessary to investigate the structure evolution with temperature in the solid solutions between Cu_2Se and Cu_2Te. **Figure 5** plots the measured heat capacity (C_p) curves for all $Cu_2Se_{1-x}Te_x$ (x= 0.2, 0.3, 0.5, 0.7) solid solutions. There is one strong peak and one wide hump in each C_p curve. Moreover, the temperatures of the peak and hump are shifted to high temperatures with increasing the Te-alloying content. All these suggest that the Se/Te ratio directly influences the phase transitions. This was further investigated by high resolution synchrotron XRD experiments at various temperatures. The multi-temperature XRD patterns for the $Cu_2Se_{0.5}Te_{0.5}$ sample are shown in Figure 5b. It is clear that the (006) diffraction peak at 4.1° disappear and the intensities of some diffraction peaks are reduced at 500 K, implying structural transformation during this process. This is consistent with the C_p curve in which the strong endothermic peak observed at 479 K. With temperature increased to 700 K, all

the diffraction peaks belong to low-temperature trigonal phase disappear. Almost all the new diffraction peaks are indexed to cubic phase except a weak reflection belongs to Cu_2O. This should be responsible for the wide hump observed in C_p curve of $Cu_2Se_{0.5}Te_{0.5}$ sample. Alieva *et al.* proposed a possible mechanism for such high temperature structural transformations in $Cu_2Se_{0.5}Te_{0.5}$.[34] At T~479 K the cubic phase nucleates at defects and then slowly grows within the low-temperature phase. Finally the phase transition reaches completion near 700 K. Such mechanism is inherent in many other chalcogenides such as $Cu_2Se_{0.5}S_{0.5}$ and ZnS.[31, 38]

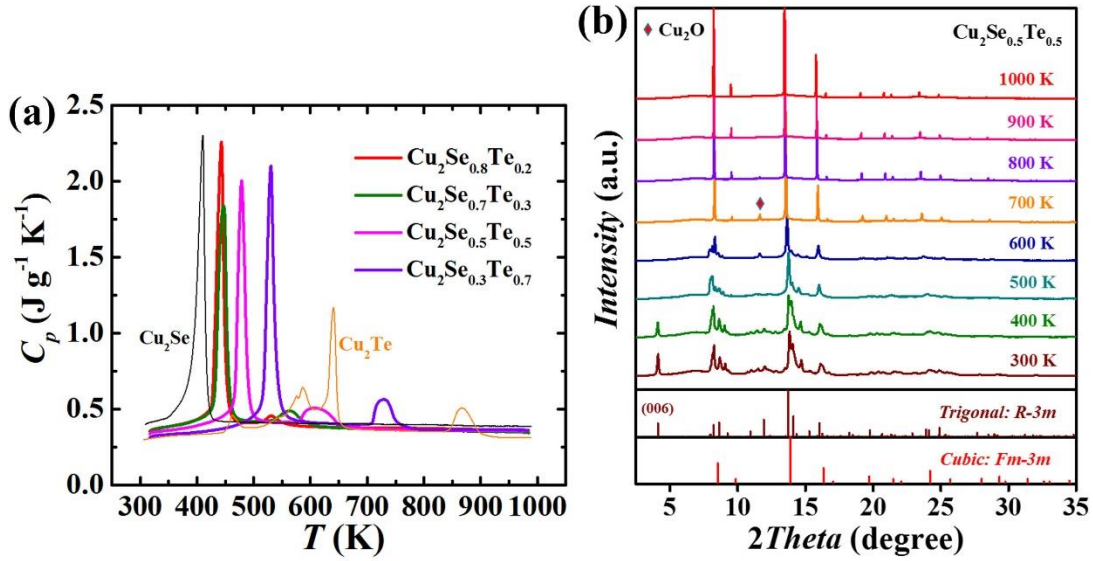

Figure 5. (a) Temperature dependence of heat capacity for $Cu_2Se_{1-x}Te_x$ (x= 0.2, 0.3, 0.5 and 0.7) solid solutions. The data of Cu_2Se and Cu_2Te are also included for comparison. **(b)** High temperature synchrotron powder X-ray diffraction patterns with a wavelength of 0.5001652 Å for $Cu_2Se_{0.5}Te_{0.5}$ measured from 300 K to 1000 K.

TE transport properties measurements were performed on the highly dense polycrystalline $Cu_2Se_{1-x}Te_x$ (x= 0.2, 0.3, 0.5 and 0.7) samples, which are showed in **Figure 6**. For comparison, Cu_2Se and Cu_2Te were prepared using the same method and their TE properties were listed in Figure 6, too. It should be noted that a very small amount of copper precipitates were observed on the surface of the ingots after annealing for all samples including Cu_2Se and Cu_2Te. These copper precipitates were removed before sintering. Thus the pellet samples actually have deviated from the nominal compositions with some copper vacancies inside the materials. The overall trend in ρ is increased with increasing temperature, showing typical heavily-doped semiconducting behavior. Besides, small discontinuous jumps between 450 K and 650 K are observed for $Cu_2Se_{0.7}Te_{0.3}$ and $Cu_2Se_{0.5}Te_{0.5}$, which are attributed to the structural transformations discussed above. The room

temperature electrical resistivity ρ for $Cu_2Se_{1-x}Te_x$ solid solutions, as well as Cu_2Se and Cu_2Te are on the order of 10^{-6} Ω m. With temperature increased to 1000 K, the resistivity of solid solutions is improved by 2-3 times while the ρ of Cu_2Se and Cu_2Te are improved by 7.4 and 3.5 times, respectively. The temperature-dependent Seebeck coefficient S of solid solutions follow the same increasing trend as resistivity, and the values are in between that of Cu_2Se and Cu_2Te matrix over the entire temperature range. Besides, the positive sign of the Seebeck coefficient indicates that holes are the dominant charge carriers, which is consistent with the intrinsic copper deficiencies in the compounds. The power factors calculated from the formula $PF\text{s} = S^2/\rho$ are shown in Figure 6c. The room temperature *PF*s for the $Cu_2Se_{1-x}Te_x$ solid solutions range from 1.5 to 3.1 μW cm^{-1} K^{-2}, which are obviously lower than that of Cu_2Se. Nevertheless, the *PF*s are greatly improved at elevated temperatures. The maximum *PF*, around 14.5 μW cm^{-1} K^{-2} at 1000 K, is obtained for $Cu_2Se_{0.8}Te_{0.2}$, which is higher than those in Cu_2Se and Cu_2Te at the same temperature.

Figure 6d presents the total thermal conductivity κ as a function of temperature for $Cu_2Se_{1-x}Te_x$ solid solutions. The data of Cu_2Se and Cu_2Te are also included for comparison. All the $Cu_2Se_{1-x}Te_x$ samples including Cu_2Se and Cu_2Te matrix show complicated temperature dependencies in the temperature range from 300 K to 1000 K due to the existence of phase transitions. At low temperatures, the lowest κ value of ~0.76 W m^{-1} K^{-1} is obtained in sample $Cu_2Se_{0.7}Te_{0.3}$, which is comparable to that of Cu_2Se. At high temperatures, the κ of solid solutions range from 0.8 W m^{-1} K^{-1} to 2.0 W m^{-1} K^{-1}, in between those of Cu_2Se and Cu_2Te. The lattice thermal conductivity (κ_L) is calculated through subtracting the charge carrier component (κ_c) from the total thermal conductivity (κ) via the relationship $\kappa_c = LT/\rho$, where L is the Lorenz number (see Figure 6e) extracted on the basis of the approximately reduced chemical potential.[39] The obtained κ_c values (see Figure 6f) of $Cu_2Se_{1-x}Te_x$ solid solutions vary from 0.4 W m^{-1} K^{-1} up to 2.0 W m^{-1} K^{-1}, which dominate the thermal conductivity. It occupies around 60% - 90% of the total thermal conductivities. All the samples exhibit extremely low lattice thermal conductivity with the values between 0.2 and 0.6 W m^{-1} K^{-1}. This is comparable to or even lower than those well-known materials with ultralow thermal conductivity.[40-43]

By combining the electronic transports and thermal conductivity, we determined the temperature dependent TE figure of merit zT (Figure 6h). Similar to the behavior of *PF*s, the zT values of $Cu_2Se_{1-x}Te_x$ are increased with increasing temperature. A maximum zT of 1.4 is obtained

at 1000 K in sample $Cu_2Se_{0.7}Te_{0.3}$. The overall zT values of $Cu_2Se_{1-x}Te_x$ solid solutions fall in between that of Cu_2Se and Cu_2Te.

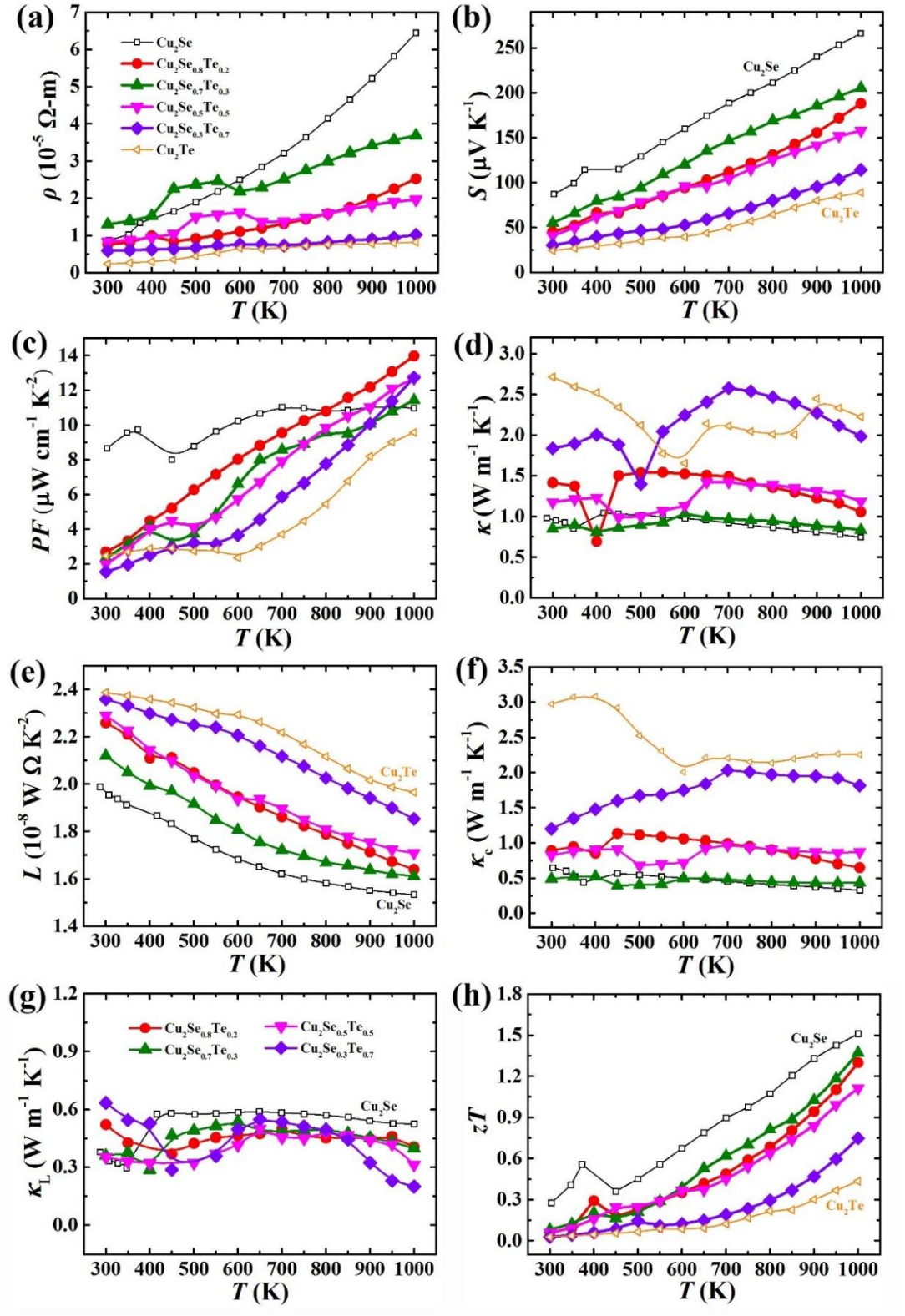

Figure 6. Temperature dependency of **(a)** electrical resistivity ρ, **(b)** Seebeck coefficient S, **(c)**

power factor *PF*, **(d)** total thermal conductivity κ, **(e)** Lorenz number *L*, **(f)** carrier thermal conductivity κ_c, **(g)** lattice thermal conductivity κ_L and **(h)** TE figure of merit *zT* for $Cu_2Se_{1-x}Te_x$ (x= 0.2, 0.3, 0.5 and 0.7). The data of Cu_2Se and Cu_2Te are also included for comparison.

To explicitly reveal the effects of Te alloying on the electrical transport properties in $Cu_2Se_{1-x}Te_x$, we carried out Hall measurements to investigate the carrier concentration and mobility for all samples at 300 K. The positive Hall carrier concentration *p*, in accord with the positive *S*, further confirms that holes are the majority carriers in $Cu_2Se_{1-x}Te_x$. Extremely high carrier concentrations, with the value up to 1.8×10^{21} cm^{-3}, are observed in Cu_2Te, which is 4 times larger than that in Cu_2Se. The carrier concentrations of $Cu_2Se_{1-x}Te_x$ solid solution fall right between that of Cu_2Se and Cu_2Te. The varied carrier concentrations are believed to be related with the chemical bond character between Cu cations and Se/Te anions. In general, weak chemical bonds easily lead to the formation of copper vacancies.[44] The electronegativity difference between Cu (1.90) and Te (2.10) is smaller than that between Cu (1.90) and Se (2.55) and the average bond length of Cu-Te is larger than that of Cu-Se. Thus Te substitution on Se sites is expected to give rise to a weak chemical bond due to the character of dominated ionic bonds between Cu and Se/Te. Besides, we have carried out the ultrasonic pulse echo measurements to evaluate the longitudinal (v_l) and shear (v_s) sound velocities, which are, usually, the indication of strength of bonding interactions.[4] As shown in **Figure 8**, both v_l and v_s are gradually decreased with increasing Te content, consistent with the argument shown above. Furthermore, our previous calculations[44] also showed the low bonding energy and thus low vacancy formation energy in Cu_2Te as compared to those in Cu_2Se or Cu_2S. Thus higher hole concentrations are observed in the materials with larger Te contents. The turnover between $Cu_2Se_{0.8}Te_{0.2}$ and $Cu_2Se_{0.7}Te_{0.3}$ could be due to the change of crystal structure. The room temperature carrier mobility μ_H of $Cu_2Se_{1-x}Te_x$ solid solutions is around 6 $cm^2\ V^{-1}\ s^{-1}$, which is obviously smaller than those in Cu_2Se and Cu_2Te. The resistivity and Seebeck coefficient as a function of Te content are shown Figure 7c and 7d. They show the opposite trend as that in carrier concentrations. This is understandable since both resistivity ρ and Seebeck coefficient *S* are inversely correlated with carrier concentration, in relation $\rho \propto \frac{1}{p}$ and $S \propto \frac{1}{p^{2/3}}$.

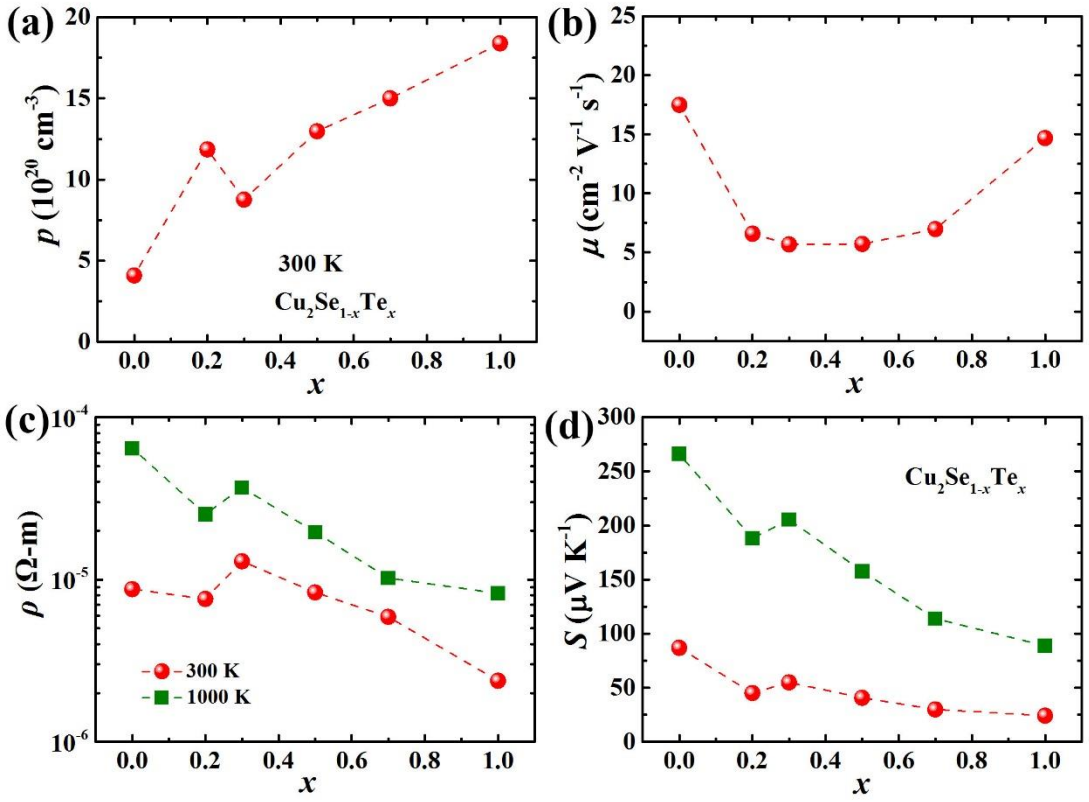

Figure 7. Electrical transport properties of $Cu_2Se_{1-x}Te_x$ (x= 0.2, 0.3, 0.5 and 0.7) as a function of tellurium content *x*. **(a)** Hole carrier concentration *p*, **(b)** carrier mobility μ_H, **(c)** electrical resistivity ρ, and **(d)** Seebeck coefficient *S*. The data of Cu_2Se and Cu_2Te are also included for comparison.

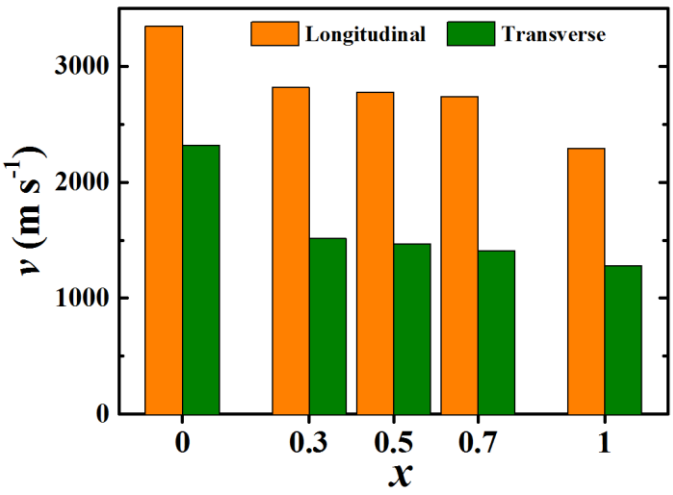

Figure 8. Longitudinal speed of sound v_l and transverse speed of sound v_t for $Cu_2Se_{1-x}Te_x$ (x =0, 0.3, 0.5, 0.7 and 1) samples.

In order to understand the effect of Te alloying on the band structure, we estimate the

effective masses m^* by using a single parabolic band (SPB) model.[45, 46] Assuming combined acoustic phonon scattering and alloy scattering are the dominated carrier scattering mechanism, the Hall carrier concentration p and Seebeck coefficient S are correlated as follows:

$$S = \frac{k_B}{e}\left[\frac{(2+\lambda)F_{\lambda+1}(\eta)}{(1+\lambda)F_{\lambda}(\eta)} - \eta\right] \quad ,(1)$$

$$p = 4\pi\left(\frac{2m^* k_B T}{h^2}\right)^{3/2}\frac{F_{1/2}(\eta)}{r_H} \quad ,(2)$$

where k_B is the Boltzmann constant, e is the elementary charge, λ is the scattering factor with a value of 0 for the combined acoustic phonon scattering and alloy scattering, and η ($=E_F/k_BT$) is the reduced Fermi energy. The Fermi integrals are given by $F_m(\eta) = \int_0^\infty \frac{x^m dx}{1+\exp(x-\eta)}$, where x is the reduced carrier energy, h is the Planck constant and r_H is the Hall factor and given by $r_H = \frac{3}{4}\frac{F_{1/2}(\eta)F_{-1/2}(\eta)}{F_0{}^2(\eta)}$. A Pisarenko plot ($S$ *vs.* p) with an effective mass m^*= 2.3 m_e (red line, m_e is the free electron mass) at 300 K is calculated according to the above expressions (see **Figure 9**). Clearly, the experimental S data of all $Cu_2Se_{1-x}Te_x$ samples including Cu_2Se and Cu_2Te fall around the red line, suggesting no obviously change in the band structure around the Fermi level.

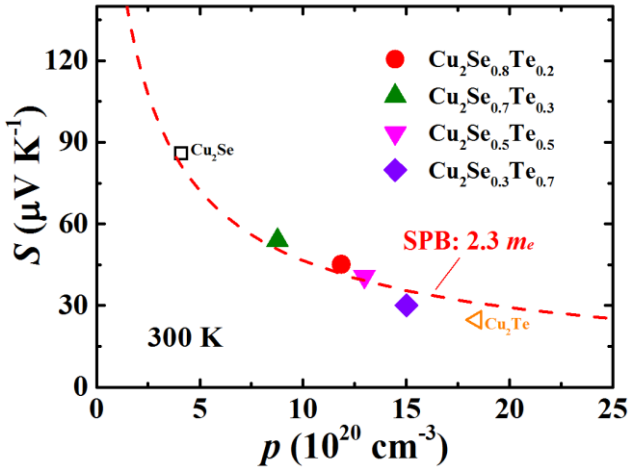

Figure 9. Pisarenko plot (Seebeck coefficients as a function of carrier concentration) for $Cu_2Se_{1-x}Te_x$ (x= 0, 0.2, 0.3, 0.5, 0.7, and 1.0) calculated by single parabolic band (SPB) model at 300 K. The symbols are experimental data.

For a given compound, the TE performance (zT) is tightly associated with its carrier concentrations but material carrier concentration has a very wide range. Material quality factor β can determine the best zT without exploring wide carrier concentration range.[47] It is comprised of several fundamental paramaters (μ_0, m^*, κ_L, and T) and given by:

$$\beta = 2\pi^{3/2} e \left(\frac{k_B}{e}\right)^2 \left(\frac{2m_e k_B}{h^2}\right)^{3/2} \frac{\mu_0 (m^*/m_e)^{3/2}}{\kappa_L} T^{5/2} \qquad .(3)$$

Here μ_0 is the mobility parameter that can be obtained by fitting the experimental data through SPB model. It is assumed the carrier concentrations do not change much at high temperatures owing to the nature of degenerate semiconductors with large band gaps. The calculated quality factor for $Cu_2Se_{1-x}Te_x$ at 1000 K is around 1.0, which is higher than most typical thermoelectric materials, as shown in **Figure 10a**. The high quality factor means excellent TE performance that could be obtained when the carrier concentration is optimized. This leads to the high zT values predicted by the SPB model (see Figure 10b). Therefore, high zT values are expected if the carrier concentrations are lowered to the optimal value through other approaches such as element doping.

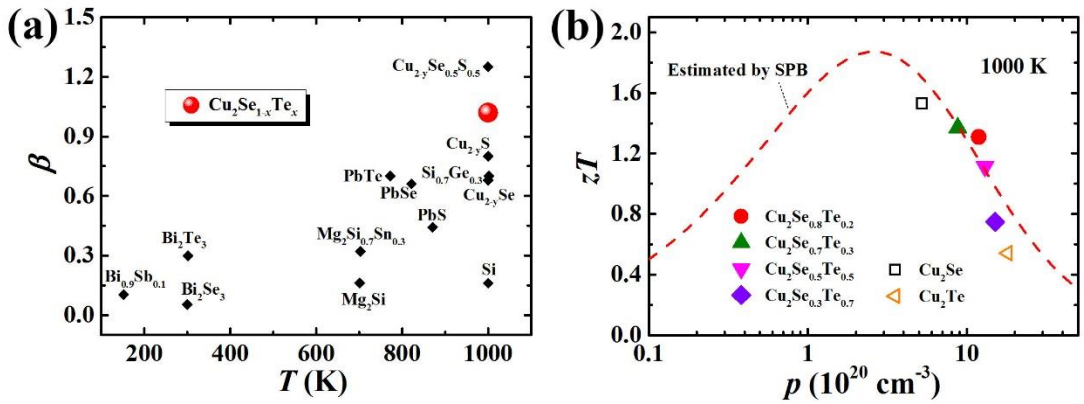

Figure 10. (a) Quality factor β for $Cu_2Se_{1-x}Te_x$. The data for a few other classic thermoelectric compounds are also included for comparison.[47] **(b)** zT as a function of Hall carrier concentration p at 1000 K. The symbols are experimental data and the curve is calculated from the single parabolic band (SPB) model.

Conclusions

In summary, a series of $Cu_2Se_{1-x}Te_x$ (x=0.2, 0.3, 0.5, and 0.7) solid solutions have been fabricated and the effects of tellurium alloying on the crystal structures and thermoelectric

properties have been systematically studied. All the $Cu_2Se_{1-x}Te_x$ solid solutions are solved in trigonal structures with space group of $R\bar{3}m$, but the Cu sites are changed for the materials with different Te-contents. Upon Te substitution at Se sites, the hole concentrations of $Cu_2Se_{1-x}Te_x$ are greatly improved due to the increased content of Cu deficiencies. Thus, both the electrical resistivity and Seebeck coefficient are much reduced when increasing Te content. Inversely, the total thermal conductivity κ for $Cu_2Se_{1-x}Te_x$ is increased due to the increased carrier thermal conductivity. The overall zT values of $Cu_2Se_{1-x}Te_x$ solid solutions fall in between those of Cu_2Se and Cu_2Te. Finally, we demonstrate that $Cu_2Se_{1-x}Te_x$ should have high thermoelectric performance if the carrier concentration can be lowered to the optimal value through other approaches such as element doping.

Acknowledgements

This work was supported by National Natural Science Foundation of China (NSFC) under the No. 51625205, Key Research Program of Chinese Academy of Sciences (Grant No. KFZD-SW-421), and Shanghai Government (Grant No. 16520721400 and 16XD1403900). B.B. Iversen thanks for the support by the Danish National Research Foundation (Center for Materials Crystallography, DNRF93), and the Danish Center for Synchrotron and Neutron Research (Danscatt).

Notes and references

1. G. Tan, L. D. Zhao and M. G. Kanatzidis, *Chem. Rev.*, 2016, **116**, 12123–12149..
2. T. Zhu, Y. Liu, C. Fu, J. P. Heremans, J. G. Snyder and X. Zhao, *Adv. Mater.*, 2017, **29**.
3. X. Shi, L. Chen and C. Uher, *Int. Mater. Rev.*, 2016, **61**, 379-415.
4. W. G. Zeier, A. Zevalkink, Z. M. Gibbs, G. Hautier, M. G. Kanatzidis and G. J. Snyder, *Angew. Chem., Int. Ed., 2016, **55**, 6826–6841*.
5. X. Shi and L. Chen, *Nat. Mater.,* 2016, **15**, 691-692.
6. C. Xiao, Z. Li, K. Li, P. Huang and Y. Xie, *Acc. Chem. Res.*, 2014, **47**, 1287-1295.
7. G. A. Slack and D. Rowe, *CRC, Boca Raton, FL*, 1995, **407440**.
8. X. Shi, J. Yang, J. R. Salvador, M. Chi, J. Y. Cho, H. Wang, S. Bai, J. Yang, W. Zhang and L. Chen, *J. Am. Chem. Soc.*, 2011, **133**, 7837-7846.
9. P. Zong, R. Hanus, M. Dylla, Y. Tang, J. Liao, Q. Zhang, G. J. Snyder and L. Chen, *Energy Environ. Sci.*, 2017, **10**, 183-191.
10. G. S. Pomrehn, A. Zevalkink, W. G. Zeier, A. van de Walle and G. J. Snyder, *Angew. Chem.*, 2014, **126**, 3490-3494.
11. E. S. Toberer, A. F. May and G. J. Snyder, *Chem. Mater.*, 2010, **22**, 624-634.
12. X. Shi, J. Yang, S. Bai, J. Yang, H. Wang, M. Chi, J. R. Salvador, W. Zhang, L. Chen and W. Wong, *Adv. Funct. Mater.*, 2010, **20**, 755-763.
13. A. Bentien, E. Nishibori, S. Paschen and B. B. Iversen, *Phys. Rev. B*, 2005, **71**, 144107.
14. H. Liu, X. Shi, F. Xu, L. Zhang, W. Zhang, L. Chen, Q. Li, C. Uher, T. Day and G. J. Snyder, *Nat. Mater.*, 2012, **11**, 422-425.

15. Y. He, T. Day, T. Zhang, H. Liu, X. Shi, L. Chen and G. J. Snyder, *Adv. Mater.*, 2014, **26**, 3974-3978.
16. L. Zhao, X. Wang, F. Y. Fei, J. Wang, Z. Cheng, S. Dou, J. Wang and G. J. Snyder, *J. Mater. Chem. A*, 2015, **3**, 9432-9437.
17. K. Zhao, H. Duan, N. Raghavendra, P. Qiu, Y. Zeng, W. Zhang, J. Yang, X. Shi and L. Chen, *Adv. Mater.*, 2017, **29**, 1701148.
18. X. Su, F. Fu, Y. Yan, G. Zheng, T. Liang, Q. Zhang, X. Cheng, D. Yang, H. Chi, X. Tang, Q. Zhang and C. Uher, *Nat. Commun.*, 2014, **5**, 4908.
19. R. Nunna, P. Qiu, M. Yin, H. Chen, R. Hanus, Q. Song, T. Zhang, M.-Y. Chou, M. T. Agne, J. He, G. J. Snyder, X. Shi and L. Chen, *Energy Environ. Sci.*, 2017, **10**, 1928-1935.
20. A. Olvera, N. Moroz, P. Sahoo, P. Ren, T. Bailey, A. Page, C. Uher and P. F. Poudeu, *Energy Environ. Sci.*, 2017, **10**, 1668-1676.
21. Y. He, T. Zhang, X. Shi, S.-H. Wei and L. Chen, *NPG Asia Mater.*, 2015, **7**, e210.
22. P. Qiu, X. Shi and L. Chen, *Energy Storage Mater.*, 2016, **3**, 85-97.
23. R. D. Heyding and R. M. Murray, *Can. J. Chem.*, 1976, **54**, 841-848.
24. A. Stevels and F. Jellinek, *Recueil des Travaux Chimiques des Pays-Bas*, 1971, **90**, 273-283.
25. S. Kashida and J. Akai, *J. Phys. C: Solid State Phys.*, 1988, **21**, 5329.
26. P. Qiu, Y. Zhu, Y. Qin, X. Shi and L. Chen, *APL Mater.*, 2016, **4**, 104805.
27. L. Yu, K. Luo, S. Chen and C.-G. Duan, *CrystEngComm*, 2015, **17**, 2878-2885.
28. E. Eikeland, A. B. Blichfeld, K. A. Borup, K. Zhao, J. Overgaard, X. Shi, L. Chen and B. B. Iversen, *IUCrJ*, 2017, **4**. 476-485.
29. M. Oliveria, R. McMullan and B. Wuensch, *Solid State Ionics*, 1988, **28**, 1332-1337.
30. Y. He, P. Lu, X. Shi, F. Xu, T. Zhang, G. J. Snyder, C. Uher and L. Chen, *Adv. Mater.*, 2015, **27**, 3639-3644.
31. K. Zhao, P. Qiu, Q. Song, A. B. Blichfeld, E. Eikeland, D. Ren, B. Ge, B. B. Iversen, X. Shi and L. Chen, *Mater. Today Phys.*, 2017, **1**, 14-23.
32. K. Zhao, A. B. Blichfeld, E. Eikeland, P. Qiu, D. Ren, B. B. Iversen, X. Shi and L. Chen, *J. Mater. Chem. A*, 2017, **5**, 18148-18156.
33. N. A. Gasimova, I. R. Amiraslanov, Y. I. Aliyev, G. G. Guseinov, M. H. Aslan, A. Y. Oral, AIP Conference Proceedings, 2011, **1400**, 476-479.
34. N. A. Alieva, G. G. Guseinov, V. A. Gasymov, Y. I. Alyev and T. R. Mekhtiev, *Inorg. Mater.*, 2015, **51**, 661-664.
35. N. Frangis, C. Manolikas and S. Amelinckx, *phys. status solidi (a)*, 1991, **126**, 9-22.
36. N. Vouroutzis, N. Frangis and C. Manolikas, *phys. status solidi (a)*, 2005, **202**, 271-280.
37. Y. G. Asadov, L. V. Rustamova, G. B. Gasimov, K. M. Jafarov and A. G. Babajev, *Phase Transit.*, 1992, **38**, 247-259.
38. J. Baars and G. Brandt, *J. Phys. Chem. Solids*, 1973, **34**, 905-909.
39. A. F. May, J.-P. Fleurial and G. J. Snyder, *Phys. Rev. B*, 2008, **78**.
40. L. Zhao, S.-H. Lo, Y. Zhang, H. Sun, G. Tan, C. Uher, C. Wolverton, V. P. Dravid and M. G. Kanatzidis, *Nature*, 2014, **508**, 373-377.
41. G. J. Snyder, M. Christensen, E. Nishibori, T. Caillat and B. B. Iversen, *Nat. Mater.*, 2004, **3**, 458-463.

42. S. Ohno, K. Imasato, S. Anand, H. Tamaki, S. D. Kang, P. Gorai, H. K. Sato, E. S. Toberer, T. Kanno and G. J. Snyder, *Joule*, 2017, DOI: 10.1016/j.joule.2017.11.005.
43. Y. Liu, L. D. Zhao, Y. Liu, J. Lan, W. Xu, F. Li, B. P. Zhang, D. Berardan, N. Dragoe, Y. H. Lin, C. W. Nan, J. F. Li and H. Zhu, *J. Am. Chem. Soc.*, 2011, **133**, 20112-20115.
44. K. Zhao, A. B. Blichfeld, H. Chen, Q. Song, T. Zhang, C. Zhu, D. Ren, R. Hanus, P. Qiu, B. B. Iversen, F. Xu, G. J. Snyder, X. Shi and L. Chen, *Chem. Mater.*, 2017, **29**, 6367-6377.
45. L. Zhao, F. Y. Fei, J. Wang, F. Wang, C. Wang, J. Li, J. Wang, Z. Cheng, S. Dou and X. Wang, *Sci. Rep.*, 2017, **7**, 40436.
46. K. Zhao, C. Zhu, P. Qiu, A. B. Blichfeld, E. Eikeland, D. Ren, B. B. Iversen, F. Xu, X. Shi and L. Chen, *Nano Energy*, 2017, **42**, 43-50.
47. H. Wang, Y. Pei, A. D. LaLonde and G. J. Snyder, in *Thermoelectric Nanomaterials*, Springer, 2013, pp. 3-32.